Vacuum 210 (2023) 111868

Contents lists available at ScienceDirect

Vacuum

journal homepage: www.elsevier.com/locate/vacuum

Improving the short-wave infrared response of strained GeSn/Ge multiple quantum wells by rapid thermal annealing

Haochen Zhao [a], Guangyang Lin [b], Chaoya Han [c], Ryan Hickey [a], Tuofu Zhama [a], Peng Cui [a], Tienna Deroy [d], Xu Feng [e], Chaoying Ni [b], Yuping Zeng [a,*]

[a] Department of Electrical and Computer Engineering, University of Delaware, Newark, 19716, Delaware, USA
[b] Department of Physics, Xiamen University, Xiamen, 361005, Fujian, China
[c] Department of Materials Science and Engineering, University of Delaware, Newark, 19716, Delaware, USA
[d] Department of Chemistry and Biochemistry, University of Delaware, Newark, 19716, Delaware, USA
[e] Surface Analysis Facility, University of Delaware, Newark, 19716, Delaware, USA

ARTICLE INFO

Handling Editor: L.G. Hultman

Keywords:
GeSn/Ge multiple-quantum-well
Molecular beam epitaxy
Thermal stability
Photodetection enhancement

ABSTRACT

In this work, the evolution of structural, optical and optoelectronic properties of coherently strained $Ge_{0.883}Sn_{0.117}$/Ge multiple quantum wells (MQWs) grown by molecular beam epitaxy under rapid thermal annealing (RTA) is systematically investigated. The MQW structure remains fully-strained state with RTA at 400 °C or below and disrupts at higher annealing temperatures due to Sn segregation and interdiffusion of Ge and Sn atoms. The GeSn well layers exhibit the strongest absorption in 2.0–2.4 μm after annealing at 400 °C and become transparent above 1.8 μm after RTA at 600 °C or beyond due to serve Sn segregation. Owing to improved crystal quality after RTA at 400 °C, the dark current of the fabricated metal-semiconductor-metal photodetector is effectively lowered by more than two times. Additionally, the responsivities at 1.55 and 2.0 μm are improved by 4.15 and 3.78 folds, respectively, compared to those of the as-grown sample. The results can be an insightful guidance for the development of high-performance short-wave infrared photonic devices based on Sn-containing group-IV low-dimensional structures.

1. Introduction

Short-wave infrared (SWIR, 1.4–3.0 μm) [1] photodetectors (PDs) are of significant interest for applications in medical imaging, spectroscopic sensing, and optical communications [2–4]. The SWIR PDs that currently dominate the market mostly rely on expensive group III-V (for example, InGaAs and InSb) and group II-VI (HgCdTe) materials [5–7]. However, the low-cost mainstream silicon (Si) based complementary metal-oxide-semiconductor (CMOS) technology are not compatible with these semiconductor materials, which prevents the integration of large-scale SWIR PDs with the Si platform in the future [8,9]. Consequently, group IV material germanium (Ge) has received more attention over the past decade [10,11]. Ge has a direct bandgap of 0.80 eV rendering Ge PDs promising for telecommunication applications [12]. However, the smaller indirect bandgap of 0.67 eV restricts its photodetection efficiency at wavelengths over 1.55 μm and sets the cutoff wavelength at around 1.8 μm [13]. Recent studies have shown that by incorporating more than ~8% α-tin (Sn) into Ge, GeSn can become a direct bandgap material [14]. By raising the Sn concentration, GeSn's bandgap can be continuously tuned from near-IR to mid-IR regions [15]. The successful demonstration of optoelectronic devices based on GeSn alloys has made possible the development of a new generation IR PDs [16–18]. In addition to the bulk GeSn, low-dimensional GeSn/Ge multiple-quantum-well (MQW) structures have been recently proposed as the suitable active region for SWIR PDs. The use of a MQW structure could increase the critical thickness of the GeSn epitaxial layers [19] and induces quantum Stark confinement effect, thus improves the optoelectronic performance [20].

The surface free energy of Sn is substantially lower than that of Ge, and the thermal equilibrium solubility of α-Sn in Ge is as low as 1% [21]. Therefore, Sn segregation is the main obstacle to homogenous GeSn alloy formation during epitaxial growth. Due to the development of ultra-high vacuum technology [22,23], non-equilibrium growth techniques are explored, such as low-temperature molecular beam epitaxy (MBE), in which GeSn can be deposited at temperatures well below the melting point of the element Sn. GeSn alloys with Sn content up to 27%

* Corresponding author.
E-mail address: yzeng@udel.edu (Y. Zeng).

https://doi.org/10.1016/j.vacuum.2023.111868
Received 8 June 2022; Received in revised form 19 January 2023; Accepted 21 January 2023
Available online 24 January 2023
0042-207X/Published by Elsevier Ltd.

have been reported, which is essential for near- and mid-IR photonics [24]. However, low-temperature MBE of GeSn alloy will lead to poor crystalline quality, which is detrimental for optoelectronic device [25,26]. Therefore, in order to grow high-quality GeSn alloy, a solution must be found to the dilemma between Sn segregation during high-temperature growth and the dense defects introduced in low-temperature growth. Post-deposition thermal annealing is an efficient method to repair point defects and relax the coherent strain [27–29]. However, the annealing temperature should be delicately controlled to avoid Sn segregation and destruction of the GeSn layer, especially for the strain-balanced GeSn/Ge MQWs [30]. Recently, some work has found RTA to be an appropriate method to improve the quality of single-layer GeSn material, such as light emission [31] and photodetection [32] performance enhancement. As for MQWs structure, several groups have investigated the effect of heat treatment on GeSn/Ge MQWs [30]. However, most of these works focused on the structural evolution of GeSn/Ge MQWs under thermal annealing [33,34]. Few studies about the effect of heat treatment on the optical and optoelectronic properties of GeSn/Ge MQWs was reported.

In this work, the influence of RTA on the structural, optical and optoelectronic properties of 10-period 16-nm $Ge_{0.883}Sn_{0.117}$/22-nm Ge MQWs are systematically investigated. High-resolution X-ray diffraction (HR-XRD), Time-of-flight secondary ion mass Spectrometer (TOF-SIMS), transmission electron microscopy (TEM), atomic force microscopy (AFM) and Raman characterizations manifest that the MQWs maintain coherently strained under RTA at 400 °C and lower. At higher annealing temperature, Sn segregation and interdiffusion of Ge and Sn take place leading to destruction of the GeSn/Ge MQWs. It is found the GeSn well layers have a largest absorption window in 2.0–2.4 μm after RTA at 400 °C and become transparent above 1.8 μm after RTA at 600 °C or beyond due to serve Sn segregation. For the fabricated metal-semiconductor-metal (MSM) photodetectors, the MQWs annealed at 400 °C shows a lowest dark current and highest responsivity due to improved crystal quality. Compared to the as-grown sample, the responsivities at 1.55 and 2.0 μm of the sample annealed at 400 °C are improved by 4.15 and 3.78 folds, respectively. These results suggest that RTA can be a beneficial technique to improve the optical and optoelectronic properties of GeSn/Ge MQWs for SWIR applications.

2. Experimental details

2.1. Preparation of GeSn/Ge MQWs

We used a Veeco/EPI Model 620 solid source MBE system with a base pressure of 2×10^{-8} Pa for the growth of Ge and GeSn materials. Ge buffer layer and GeSn/Ge MQW structures were grown epitaxially on 3-inch p-type Si (001) wafers with a resistivity of 3–10 Ω cm. The Ge and Sn beams were formed by thermal evaporation of triple zone-refined intrinsic polycrystalline Ge and a high purity (99.9999%) metallic Sn source. The growth rate and composition of the GeSn alloy were controlled by adjusting the temperature of the effusion cells. The Si substrate was cleaned with an optimized RCA wet-chemical procedure [35]. Afterward, the substrate was loaded into the main chamber and underwent a degassing process. A Ge buffer layer was growth using a two-step low-temperature/high-temperature (LT-HT) growth process, which involved depositing a Ge seed layer at 330 °C and growing a high-quality Ge film at 600 °C. After depositing the Ge layer at a high temperature, in-situ annealing was performed at 850 °C to reduce the threading dislocation defects (TDDs). The final Ge buffer layer thickness was 570 nm after repeating all three steps. The GeSn/Ge MQWs structure consists of 10 periods of 16 nm $Ge_{0.883}Sn_{0.117}$ and 22 nm Ge grown at 150 °C to avoid Sn segregation and maximize Sn incorporation. The final thickness of each layer of the GeSn/Ge MQWs sample was determined using TEM Talos F200C in the cross-section geometry. Each layer's thickness and Sn composition were also validated by simulated the XRD rocking curves and SIMS measurements.

2.2. RTA of GeSn/Ge MQWs and fabrication of MSM PDs

The RTA was performed at a temperature range from 200 to 800 °C for 1 min under a nitrogen (N_2) atmosphere. Each sample was patterned with Ti/Au(170/80 nm) interdigitated finger contacts by a standard lift-off process. Before metal deposition, 12.5% dilute hydrochloric acid (HCl) was used to remove surface oxides to form ohmic contacts. The pattern used for these devices is a set of interdigitated finger contacts with an active area of 1700 μm × 750 μm.

2.3. Characterizations of GeSn/Ge MQWs

The surface morphology and microstructure of the films were characterized by AFM and TEM. Raman spectra and XRD rocking curves were used to characterize the material quality of the MQWs. XRD rocking curves were obtained by Bruker HR-diffractometer D8. Raman spectroscopy experiments were performed at room temperature using the Thermo Scientific DXR 3 Raman Microscope equipped with a 532 nm laser. The incident light was focused on the sample surface with a laser spot size of 0.7 μm with a magnification of 50 ×. The laser power was 1 mW. XPS (X-ray photoelectron spectroscopy) was used in this study with the aim of analyzing the effects of the RTA gas treatment conditions and HCl treatment on the GeSn surface. The XPS spectrometer is Thermo Fisher K-Alpha XPS. The base pressure during spectra acquisition was lower than 1E-5 Pa. The excitation source was a monochromated Al Kα (1486.6 eV). The spot size of X-ray beam was 400 μm. All spectra were collected at the normal emission angle. During spectra acquisition, the charge neutralizer (electron flood gun) was used. TOF-SIMS measurements were utilized to quantify Ge, Sn concentrations using TOF SIMS 5 (ION TOF, Inc. Chestnut Ridge, NY). The SIMS measurement setup and SIMS calibration procedure to obtain Sn concentrations can be found in the Supplementary material. A Thermo Fisher iS50R Fourier transform infrared (FTIR) spectrometer was employed to measure the absorption spectra of samples annealed at different temperatures. Data were collected using a liquid-nitrogen cooled MCT photodetector that operated at wavelengths between 1.43 μm and 22 μm [1]. All current-voltage (I-V) characteristics were measured by a Keithley 2450 source meter. The spectral responsivity of fabricated MSM PDs under IR blackbody light source illumination at different biases was characterized by the FTIR. The Lock-in technique was employed to improve the signal-to-noise ratio by an SR860 500 kHz DSP lock-in amplifier from Standard Research Systems and an MC100 optical chopper from Thorlabs. A 1.55 μm Fabry-Perot Laser diode FPL1055T controlled by a laser diode controller LDC205C and a temperature controller TED200C was used to calibrate the responsivity of all the devices. The optical power from a 1.55 μm laser was measured by a StarLite laser power and energy meter as well as a high sensitivity thermal laser sensor 3A from Ophir.

3. Results and discussion

3.1. Structure and morphology analysis

Fig. 1 shows the TEM image of the GeSn/Ge MQWs grown on a Ge virtual substrate. In the MQWs region, abrupt and flat interfaces between the GeSn wells and the Ge barriers without dislocation regions can be observed, proving the high quality of the GeSn/Ge MQWs structure. The inset shows a magnified TEM image of the interface between the GeSn well layer and the Ge barrier layer. The thicknesses of the GeSn well layer and the Ge barrier layer are ~16 nm and ~22 nm, respectively.

Typical 5 × 5 μm^2 AFM images of GeSn/Ge MQWs as-grown and annealed samples are shown in Fig. 2 (a)-(h). The surface roughness root mean square (RMS) of each sample as a function of RTA temperature is shown in Fig. 2 (i). The surface of samples annealed at temperatures below 400 °C is smooth as evidenced by the RMS roughness in the range of 1.04–1.38 nm, indicating no Sn dots on the surface. For the samples

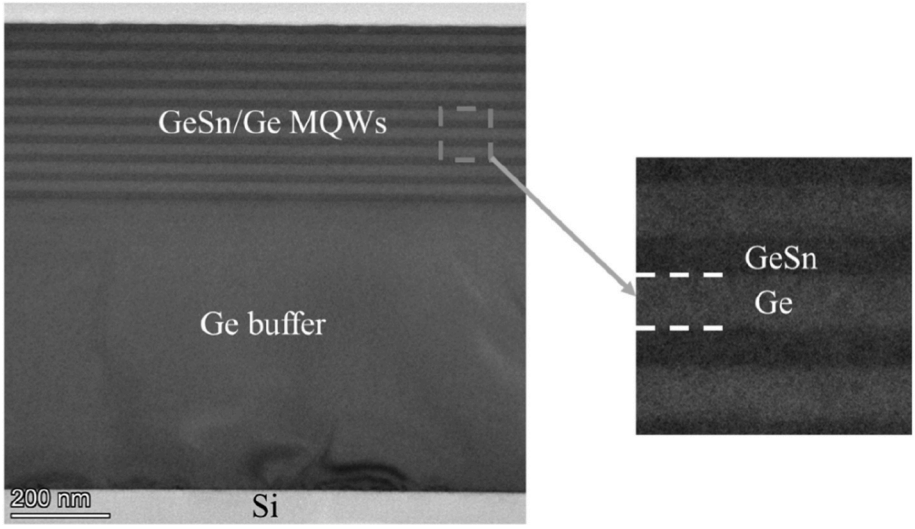

Fig. 1. Cross-sectional TEM image of as-grown GeSn/Ge MQWs on Ge/Si virtual substrate (Inset is a magnified view of TEM image of GeSn/Ge interface region).

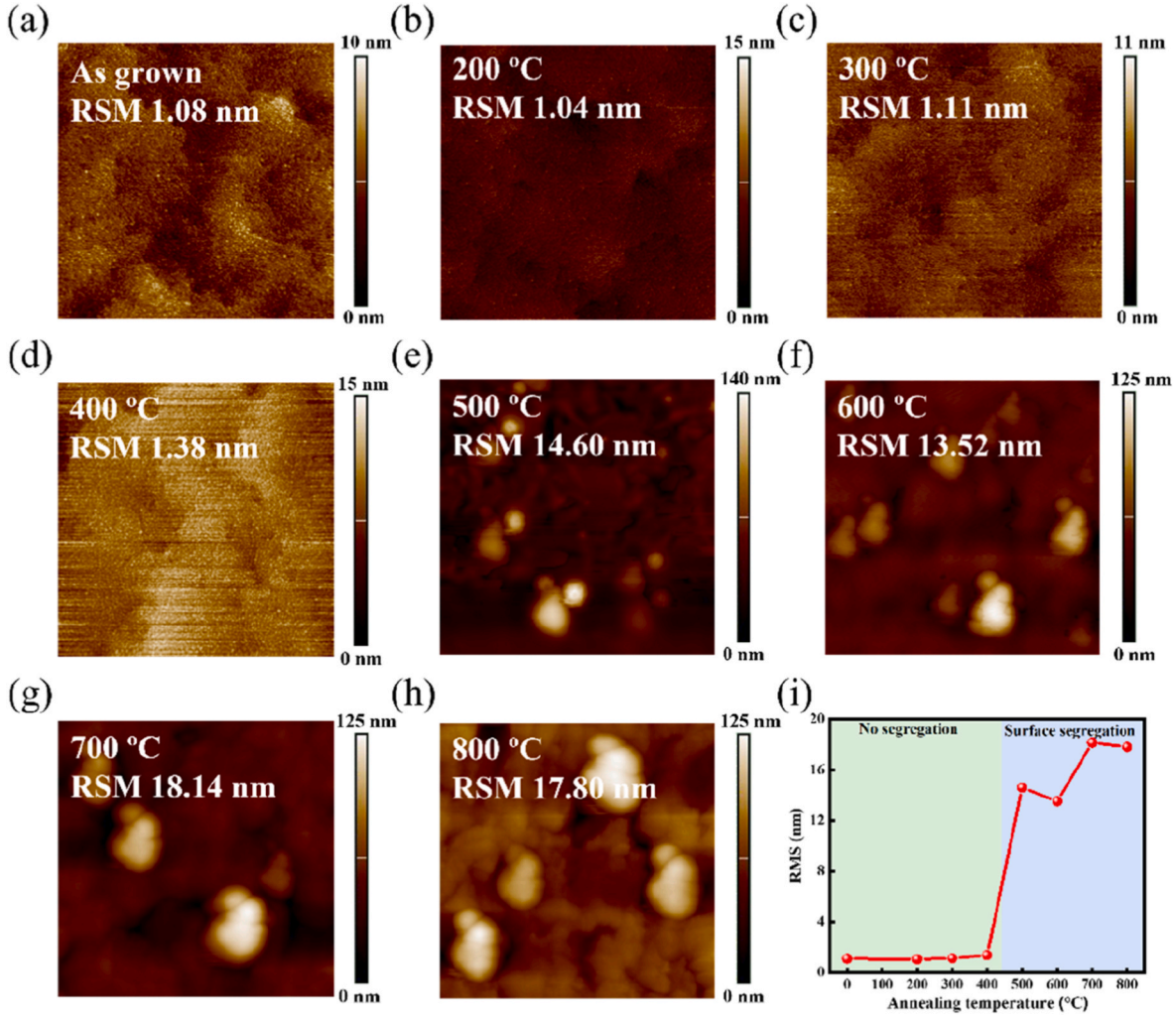

Fig. 2. (a)–(h) AFM images (5 × 5 μm^2) of GeSn/Ge MQWs samples after RTA at different temperatures. (i) RMS surface roughness of GeSn/Ge MQWs samples as a function of RTA temperature.

annealed higher than 500 °C, surface roughness increases dramatically because Sn dots appear on the surface, implying a severe loss of Sn atoms in the GeSn layer.

In order to shed light on the crystal quality, (004) XRD scans were performed on the as-grown samples as shown by the black lines in Fig. 3. The existence of well-defined Pendellösung interference fringes

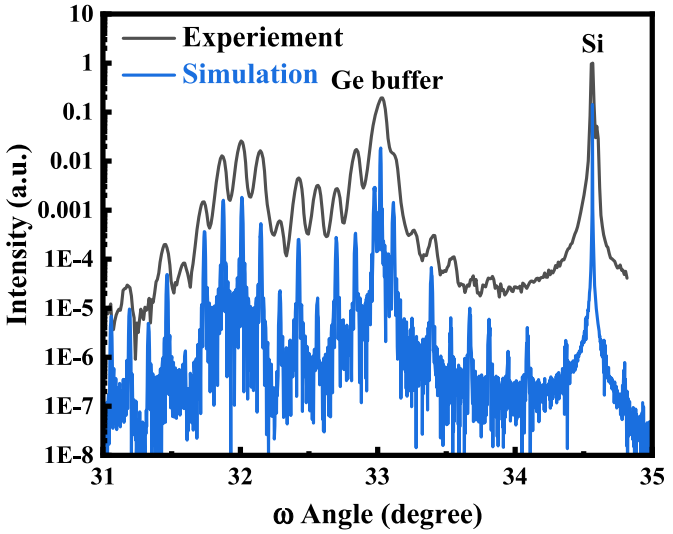

Fig. 3. Measured and simulated symmetric (004) XRD curves of the $Ge_{0.883}Sn_{0.117}$/Ge MQWs grown on a relaxed Ge/Si virtual substrate. The two main peaks correspond to Si substrate and Ge buffer.

demonstrates the abruptness of the GeSn/Ge MQWs interface and the high quality of the epitaxial layers [33]. The periodic oscillations of the satellite peaks represent the presence of periodicity and good epitaxial layer thickness uniformity of the MQWs. The structure of the GeSn/Ge MQWs is simulated with X'Pert Epitaxy software based on the structural and compositional parameters calculated from the ω/2θ scan of the (004) reflection, and the blue line shows the results in Fig. 3. The thicknesses of the GeSn well layer and the Ge barrier layer are determined to be 16 nm and 22 nm, respectively, in agreement with the values obtained from TEM. The extracted Sn composition in the GeSn well layer is about 11.7%.

Fig. 4 shows the XRD results of ω/2θ scans of the (004) reflections for the GeSn/Ge MQWs samples after treatment by RTA for 1 min in a N_2 atmosphere over a wide temperature range of 200°C-800 °C. Initially, there is no distinguishable change in the position of the XRD peaks with increasing RTA temperature. The peaks for samples with annealing temperatures below 400 °C for 1 min are highly identical to the sample without RTA, and the interference peaks remain well defined. For the samples annealed below 400 °C, the results of the XRD and AFM measurements almost remain unchanged, indicating that the crystal structure remained unchanged. This also indicates that the GeSn/Ge MQWs have good thermal stability from 200 °C to 400 °C. Fig. 5 (a) and (b) show the atomic distribution of Ge and Sn along the growth direction from the surface to the Ge buffer layer for as-grown sample and sample annealed at 400 °C. In the MQW region, periodic variations can be observed in the atomic distributions of Ge and Sn, which correspond to GeSn wells and Ge barriers. In addition, the thickness of each layer is in agreement with our TEM results. The Sn concentration in the GeSn wells is determined to be 11.6% based on the SIMS data (see the Supplementary material), which is in agreement with the 11.7% Sn concentration extracted from the XRD simulation. Both samples show the same atomic distribution of Ge and Sn, indicating that there is no Sn segregation and GeSn/Ge quantum well destruction, agreeing well with previous AFM and XRD measurements. Intriguing changes are seen when the RTA temperature is raised to 500 °C or higher. The interference peaks start to vanish, showing that the RTA process leads to the destruction of the MQWs caused by Sn segregation and interdiffusion of Ge and Sn atoms [32]. At the same time, according to the AFM results, Sn dots started to appear on the surface. As the annealing temperature increases from 600 °C to 800 °C, GeSn peak merging with the Ge peak appears as a shoulder of the Ge signal, pointing to the sudden appearance of Sn segregation. After RTA at 800 °C, the XRD pattern remains the

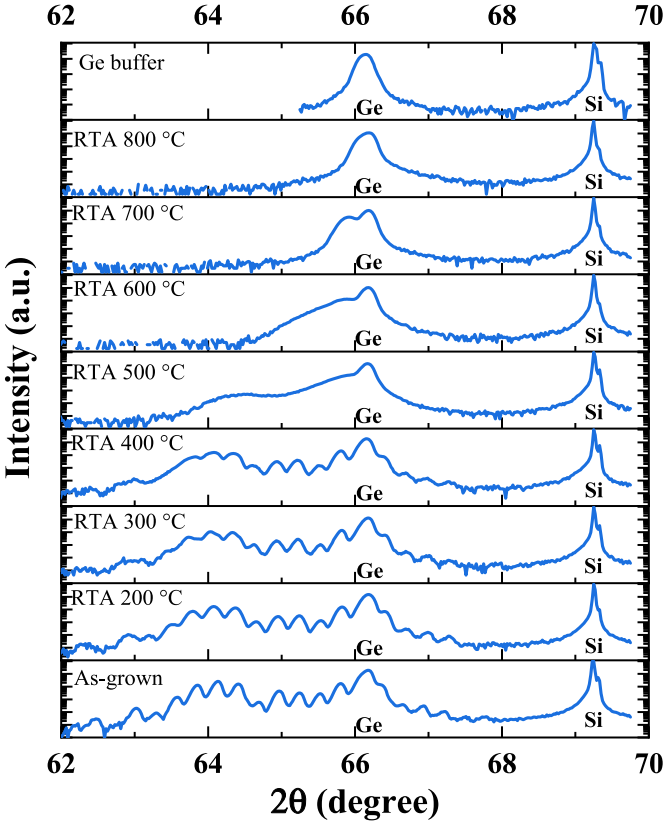

Fig. 4. (004) XRD scans of as-grown GeSn/Ge MQWs sample, and the samples annealed ranging from 200 °C to 800 °C under a N_2 atmosphere by RTA for 1 min.

same as that of the 570 nm thick relaxed Ge virtual substrate sample, which indicates severe Sn segregation.

Fig. 6 (a) shows the normalized Raman spectra of the as-grown, RTA annealed samples and a bulk Ge (001) reference wafer. An intense peak is observed in all samples, which is attributed to the Ge–Ge longitudinal optical (LO) peak [36]. The broadening of the Ge–Ge peak is due to the fluctuations in composition and the crystalline quality of the material [37]. In Fig. 6 (b), the Ge-Ge peak and Ge-Sn peak from the as-grown sample are observed and their positions are extracted by fitting a multi-peak curve using a Gaussian function. The detailed Raman shift values of the Ge-Ge and Ge-Sn peaks for all samples can be seen in Fig. 6 (c). The Ge-Ge peak position around 300 cm^{-1} does not change for samples with RTA temperatures up to 800 °C. For the samples annealed at the temperature ranging from 500 °C to 700 °C, the Ge-Sn peak shifted to 294 cm^{-1} due to the Sn segregation. The Ge-Sn peak diminishes for the sample annealed at 800 °C due to the severe Sn segregation. This result is consistent with the XRD results of the sample annealed at 800 °C. Full width at half maximum (FWHM) is a significant parameter that gives important information about the crystalline quality of thin films [37]. Therefore, the FWHM of the measured peaks for all samples is plotted as shown in Fig. 6 (d), where it can be seen that the FWHM decreases with increasing RTA temperature. While the annealed samples show lower values, the as-grown sample has the highest FWHM. The annealed samples' lower FWHM values show that the heat treatment has improved the film's crystalline quality. However, for the samples annealed above 500 °C, the decrease in FWHM values is caused by Sn segregation as verified by the AFM and XRD results. From the Raman FWHM results, we can deduce that the crystalline quality of the GeSn/Ge MQWs layers gradually improves without MQWs structure change and Sn segregation when RTA temperature is below 400 °C. Therefore, an appropriate heat treatment condition is essential to further enhance the

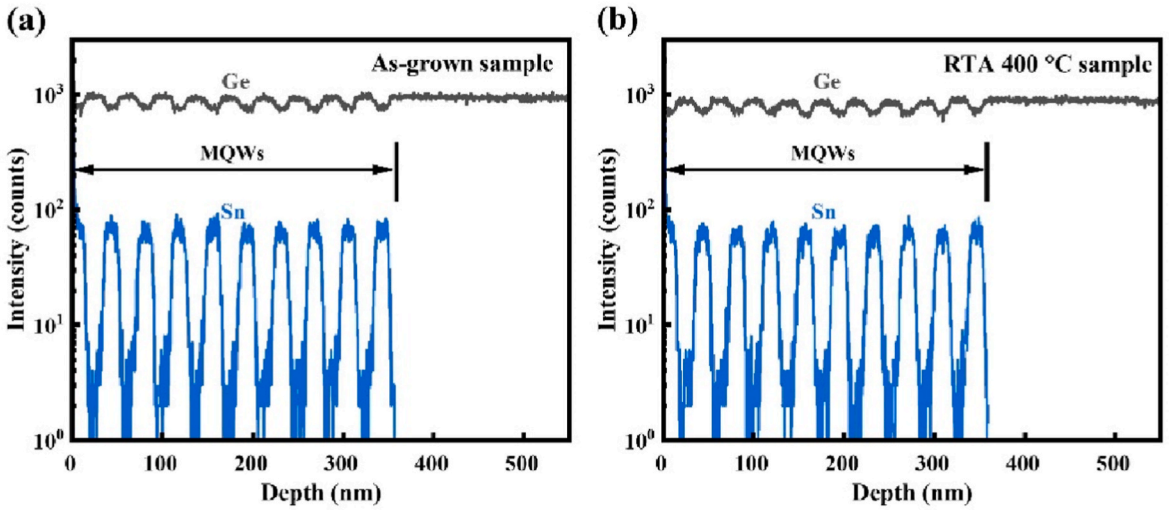

Fig. 5. SIMS depth profile of Ge and Sn elements in the GeSn/Ge MQW structure from the surface to the Ge buffer layer of (a) as-grown sample and (b) sample annealed at 400 °C under a N_2 atmosphere by RTA for 1 min.

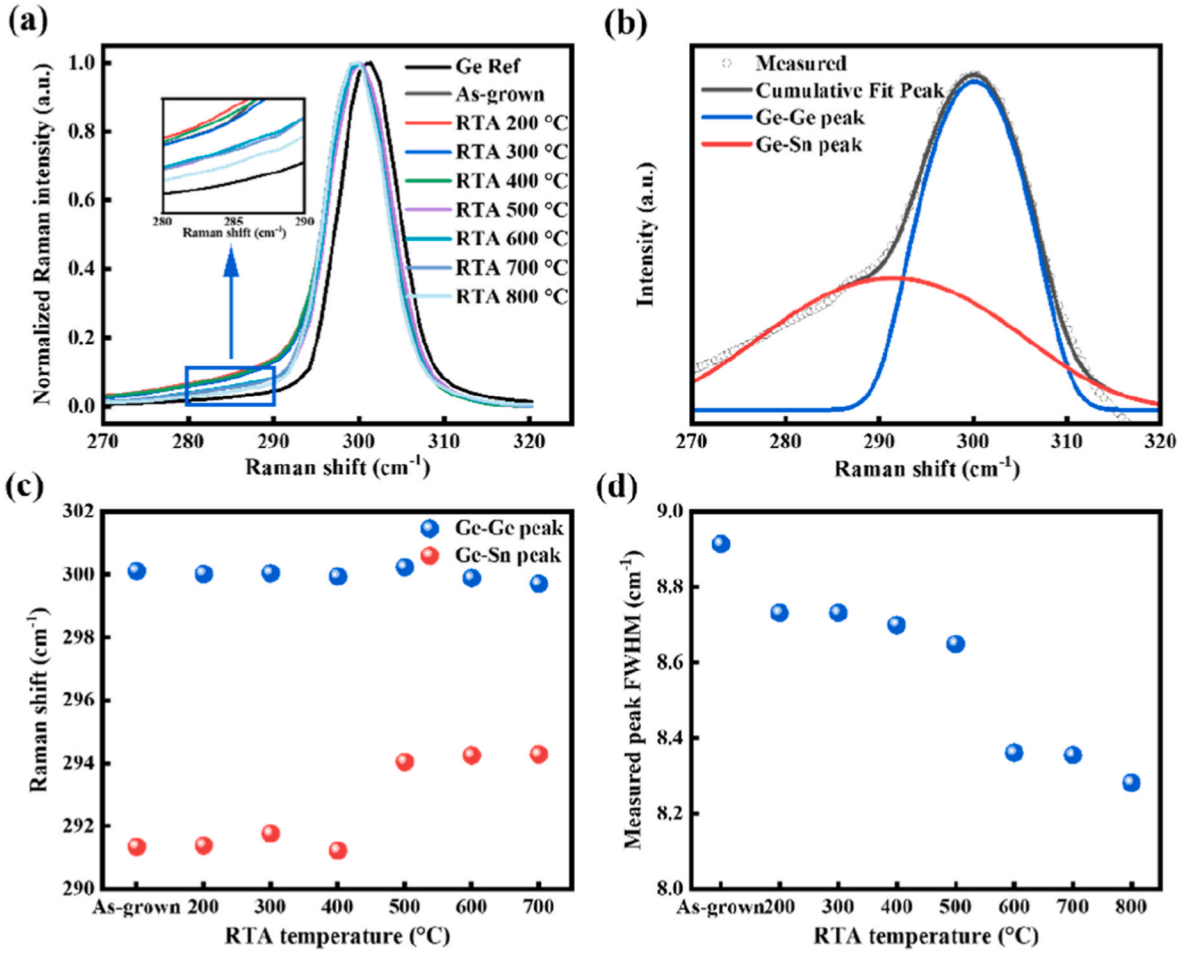

Fig. 6. (a) Raman spectra of bulk Ge, as-grown sample, and the samples annealed ranging from 200 °C to 800 °C (Inset shows a magnified view of the region demonstrating the Raman shift difference among all samples); (b) A semi-log plot of the Raman spectrum of an as-grown sample with fitting results that resolve the Ge–Ge peak at approximately 300 cm^{-1} and a clear shoulder at approximately 291 cm^{-1}; (c) Detailed Ge-Ge peak and Ge-Sn peak as a function of RTA temperature; (d) Corresponding full width at half maximum (FWHM) values of the measured peaks as a function of RTA temperature.

material quality while maintaining the structural integrity of the MQWs structure.

Samples were stored in nitrogen atmosphere for two months prior to the XPS measurements. For the samples treated with HCl solution, 12.5% dilute HCl, acetone and isopropanol (IPA) were applied to the sample surface to remove surface oxides and contaminants before

transferring to the XPS chamber. The time required to transfer the HCl-treated samples from the chemical solution to the XPS chamber was kept below 30 min in order to minimize the substantial oxidative regeneration. For materials exposed to the air, the nature of the adventitious carbon (AdC) peak with carbon contamination on the surface depends on the substrate, the environment, and the exposure time [38]. In our study, we performed the binding energy referencing process by analytically examining the C $_{1s}$ peak of AdC comprehensively. The binding

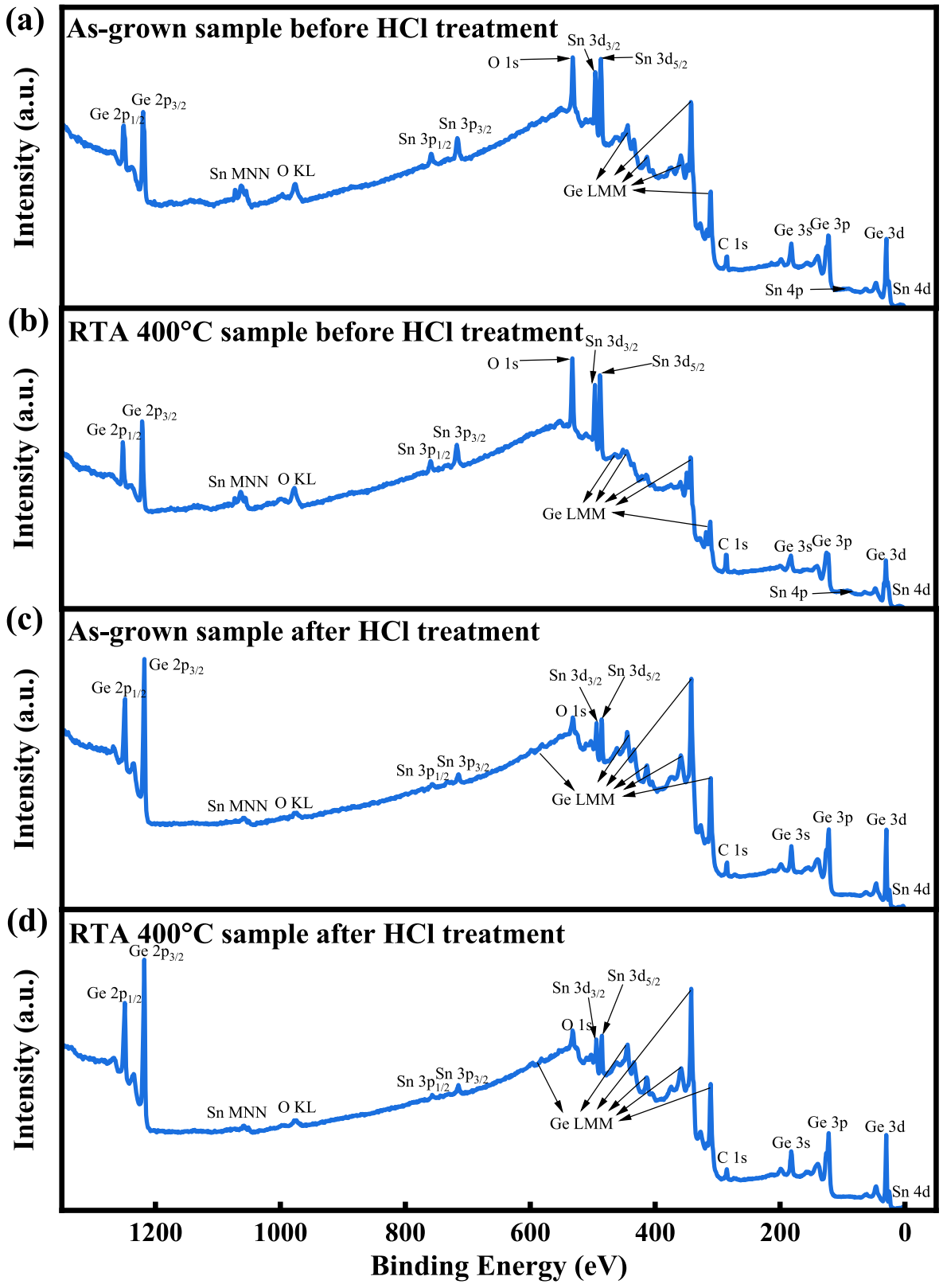

Fig. 7. Overall XPS survey spectrum recorded from the $Ge_{0.883}Sn_{0.117}$/Ge MQWs (a) as-grown sample, (b) sample annealed at 400 °C, (c) as-grown sample after HCl solution treatment and (d) sample annealed at 400 °C after HCl solution treatment.

energy (EB) of the C-C/C-H peak of AdC depends on the work function/electron affinity (Φ_{SA}) of the deposited sample. The sum of EB and Φ_{SA} is a constant value, indicates that C $_{1s}$ does not change with respect to the vacuum level [39]. The electron affinity of 11.7% GeSn alloys is around 4.32 [40]. The C $_{1s}$ peak of the AdC was then set to 289.58 - Φ_{SA} eV (285.26 eV) [41,42]. All core levels were calibrated referred to the C $_{1s}$ component at 285.26 eV. All peaks were fitted using Avantage software. Fig. 7 (a)-(d) show overall XPS survey spectrum recorded from the $Ge_{0.883}Sn_{0.117}$/Ge MQWs as-grown sample, sample annealed at 400 °C, as-grown sample after HCl solution treatment and sample annealed at 400 °C after HCl solution treatment. The presence of only four elements (Ge, Sn, C and O) on the surface is confirmed by the photoemission peak patterns matching these elements. Fig. 8 (a)-(d) show the C $_{1s}$, Ge $_{3d}$, Sn $_{3d}$ and O $_{1s}$ XPS spectra of the as-grown sample, the as-grown sample after HCl solution treatment, the sample annealed at 400 °C and the sample annealed at 400 °C after HCl solution treatment. XPS spectra of C $_{1s}$, Ge $_{3d}$ and Sn $_{3d}$ were normalized on energy scales from 282 to 292 eV, 21–35 eV and 482–498 eV. In addition, Figs. S2–S5 in the supplemental material show measured and fitted peaks for all major core-level spectra including C $_{1s}$, Ge $_{3d}$, O $_{1s}$ and Sn $_{3d}$. As shown in Fig. 8 (a), the C $_{1s}$ peak of the AdC was set to 285.26 eV. As can be seen from Fig. 8 (b) and (c), after RTA treatment, the intensity of GeO_x and SnO_x peaks increased, an indication of the growth of surface oxides and possible surface contamination under RTA N_2 gas treatment conditions. Meanwhile, the HCl treatment can effectively remove the surface oxides and surface contamination formed during the RTA process. The Ge $_{3d}$ XPS spectra of the as-grown sample and the sample annealed at 400 °C after HCl treatment showed the presence of one Ge $_{3d}$ peak but the missing of GeO_x peak. A similar story is shown in the Sn $_{3d}$ spectra, indicating the presence of the Sn $_{3d3/2}$ and $Sn_{3d5/2}$ peak but the absence of SnO_x peak. Fig. 8 (d) shows that the intensity of the O $_{1s}$ peak is significantly reduced after HCl solution treatment, which also implies that HCl solution treatment can effectively remove the oxides from the surface. After HCl solution treatment, the O $_{1s}$ peak still has a weak intensity, which may be attributed to the brief time of exposure to air during transferring to the XPS chamber after HCl solution treatment. From the above XPS measurements, there is not much difference between as-grown sample after HCl solution treatment and the sample annealed at 400 °C after HCl solutions treatment, which indicates that the improvement of the short-wave IR optical response comes from the change of the GeSn/Ge MQWs material quality rather than from the effect of surface oxides and surface contamination due to the RTA process.

3.2. Optical and optoelectronic properties

Fig. 9 shows absorption spectra for wavelengths ranging from 1.5 μm to 2.6 μm. Because the edge of Ge absorption is around 1.85 μm [43], the peak at 1.6 μm is considered as the absorption mainly from Ge epitaxial layers. In addition, another broadened peak can be observed in the wavelength range of 1.8 μm and 2.6 μm which is attributed to the GeSn absorption. We can clearly see that the sample annealed at 400 °C has the highest peak intensity, which indicates a higher absorption signature in the wavelength range of 1.8 μm and 2.6 μm due to the crystal quality improvement as compared to other samples, agreeing well with Raman's

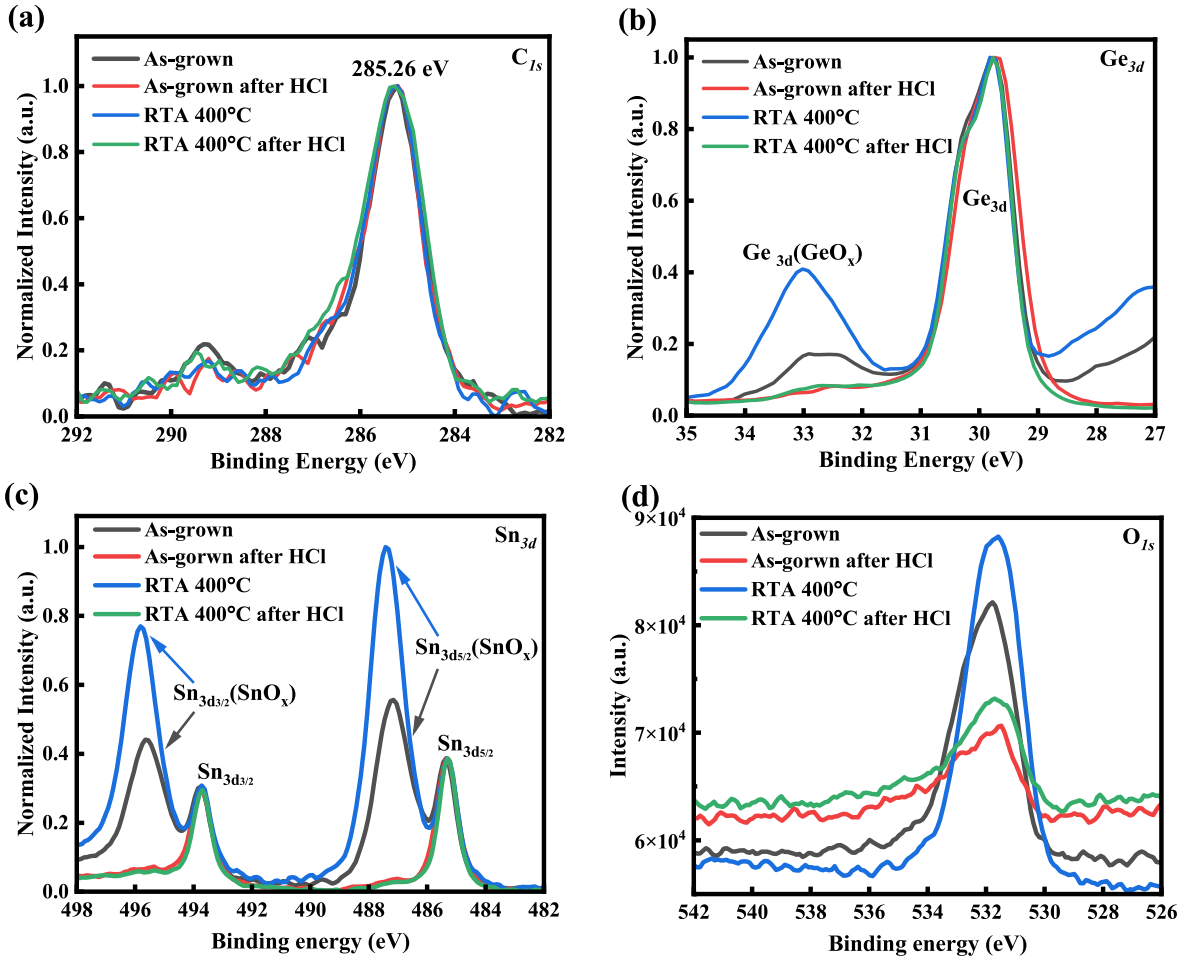

Fig. 8. Measured (a) C $_{1s}$, (b) Ge $_{3d}$, (c) Sn $_{3d}$ and (d) O $_{1s}$ XPS spectra of the $Ge_{0.883}Sn_{0.117}$/Ge MQWs as-grown sample, as-grown sample after HCl solution treatment, sample annealed at 400 °C and sample annealed at 400 °C after HCl solution treatment.

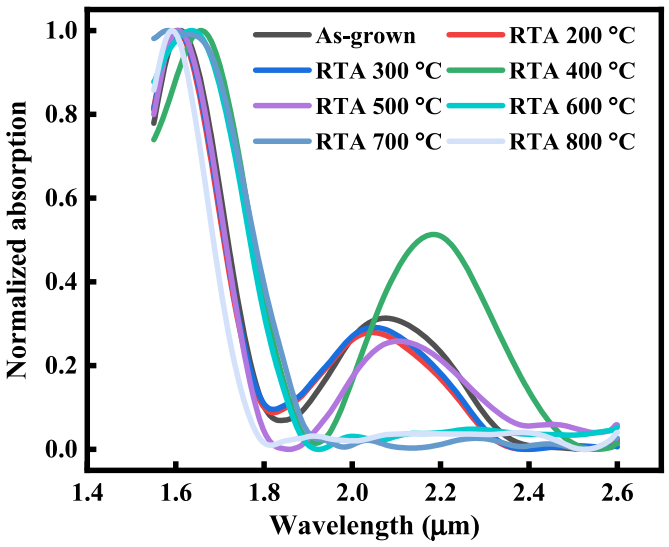

Fig. 9. Room-temperature absorption spectra of the as-grown sample, and the samples annealed at temperatures ranging from 200 °C to 800 °C.

FWHM results. The sample annealed at 400 °C exhibited an absorption edge of about 2.5 μm while the as-grown sample and annealed at 200 °C, 300 °C and 500 °C exhibit a value of 2.40 μm. According to the PDs responsivity results (to be shown in Fig. 11), the absorption edge for the sample annealed at 400 °C is closer to the PDs responsivity cut-off wavelength value. The difference in absorption and PDs responsivity cutoff wavelengths for the as-grown sample and annealed at 200 °C, 300 °C and 500 °C may be due to the absorption signal at the wavelength ranging from 2.4 μm to 2.6 μm being weaker than what the MCT detector can detect. For samples annealed above 500 °C, as the annealing temperature rises from 500 °C to 800 °C, the absorption peak gradually disappears and the absorption edge gradually moves to shorter wavelengths (from 2.4 μm to 1.8 μm), which is attributed to the gradual segregation of Sn, consistent with the above-mentioned AFM, XRD and SIMS results.

The cross-sectional schematic of the GeSn/Ge MQWs MSM PDs is shown in Fig. 10 (a). A top view microscope picture of a typical GeSn/Ge MQWs MSM PD is shown in Fig. 10 (b). Fig. 10 (c) presents the current-voltage characteristics of the fabricated MSM PDs under dark conditions. Fig. 10 (d) shows the dark currents of the GeSn/Ge MQWs PDs at 1 V bias. Among all the samples, the devices based on GeSn/Ge MQWs annealed at 400 °C sample has the lowest dark current. The suppression of the dark current is attributed to the improved material quality as verified by the above-mentioned Raman, absorption and SIMS measurements results.

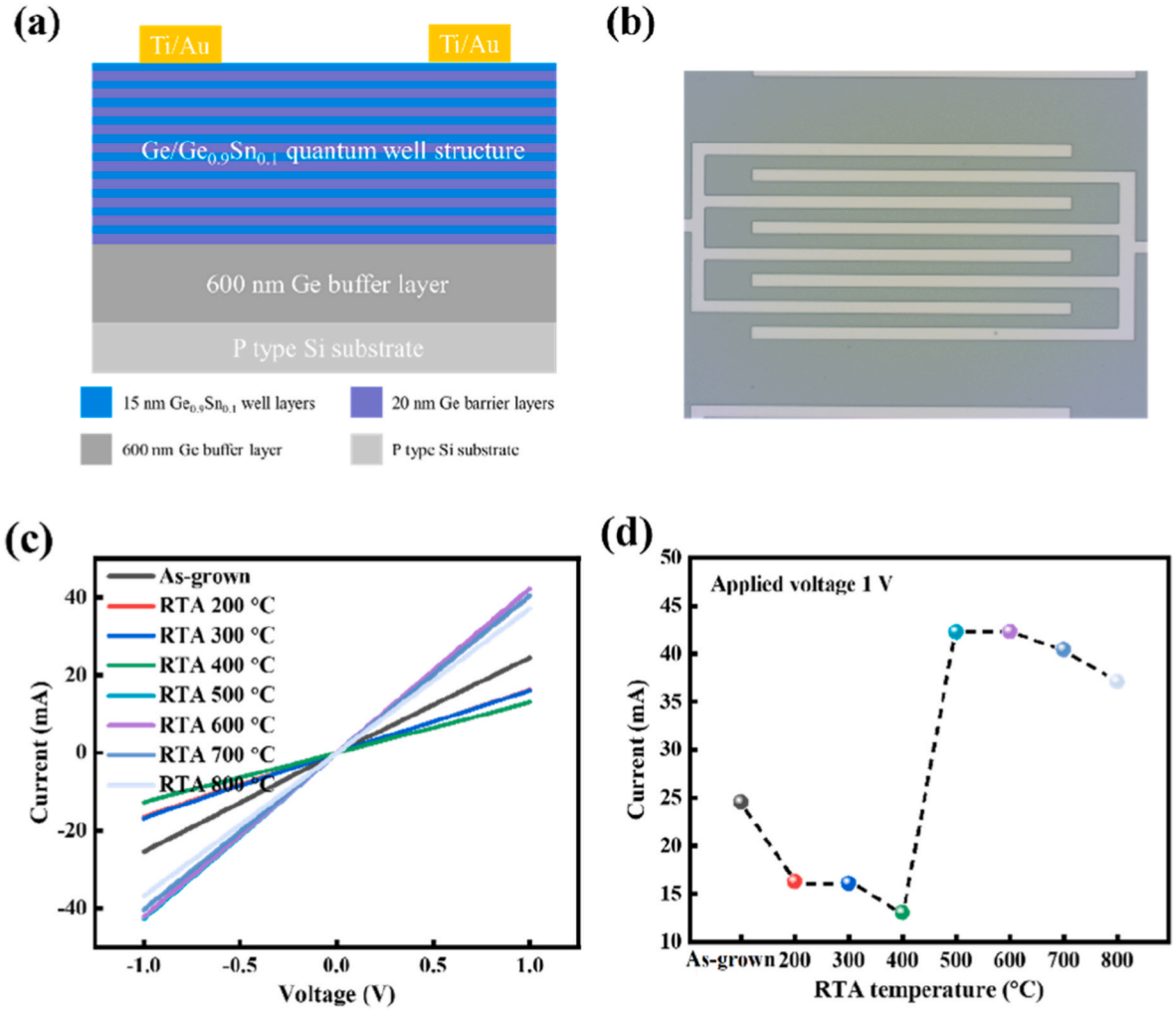

Fig. 10. (a) Cross-sectional schematic of the GeSn/Ge MQWs MSM PDs; (b) Microscope image of the top view of a GeSn/Ge MQWs MSM PD; (c) Current-Voltage characteristics of the GeSn/Ge MQWs PDs under the dark condition; (d) Dark currents of the GeSn/Ge MQWs PDs at 1 V bias.

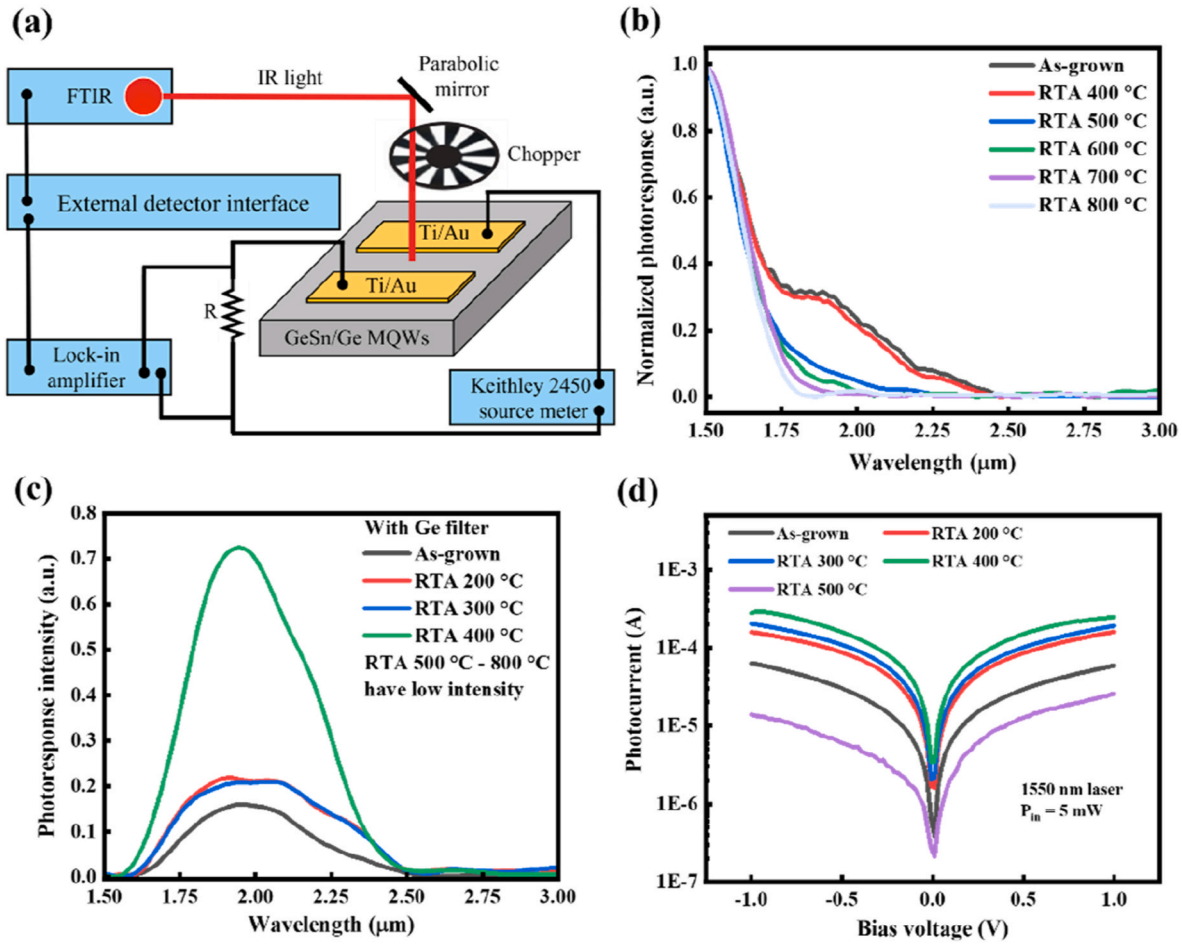

Fig. 11. (a) Schematic measurement setup used to measure the spectral response of the GeSn/Ge MQWs MSM PDs. (b) Spectral response of the GeSn/Ge MQWs MSM PDs based on the as-grown sample, and the samples annealed from 400 °C to 800 °C. (c) The spectral response with Ge filter of the GeSn/Ge MQWs MSM PDs based on the as-grown sample, and the samples annealed from 200 °C to 400 °C. (d) Photocurrent–Bias voltage characteristics of GeSn/Ge MQWs MSM PDs based on the as-grown sample, and the samples annealed from 200 °C to 500 °C under incident light with P_{in} = 5 mW at λ = 1.55 μm.

The spectral photocurrents were measured in amplitude modulation (AM) step-scan mode with an FTIR spectrometer fitted with an IR black body source. A Calcium Fluoride (CaF_2) beam splitter was selected because of its favorable near-IR response. The samples were connected in series with a matching resistor and received a DC bias voltage. A two-inch parabolic mirror with a four-inch focal length focused the IR black body source on the sample. The photocurrent from the GeSn/Ge MQWs MSM PDs at the bias of 1 V was then transferred to a current amplifier. The signal was then sent back to the external detector interface of the FTIR. A mechanical chopper wheel tuned to 278 Hz was used to phase-lock the photocurrent and suppress broadband noise, and the signal was fed to the FTIR through the lock-in amplifier. The internal deuterated triglycine sulfate (DTGS) in the FTIR which has a wavelength-independent responsivity, was utilized to calibrate the relative intensity of the IR blackbody light source. A Schematic diagram of the spectral response measurement setup is shown in Fig. 11 (a). Spectral responses of the photoconductors were characterized in the 1.4 μm–4.0 μm wavelength range. The devices' responses were normalized at 1.5 μm to facilitate the fair comparison at longer wavelengths. The obtained normalized FTIR spectra are shown in Fig. 11 (b). For the samples annealed below 400 °C, including the as-grown samples, the cutoff photo-response wavelengths remained almost unchanged around 2.5 μm. This result is consistent with the absorption spectra, especially when compared to the absorption edge for samples annealed at 400 °C (2.5 μm). However, as the annealing temperature increases from 500 °C to 800 °C, the cutoff wavelength gradually shifts from 2.5 μm to a shorter wavelength of 1.85 μm. For the sample annealed at 800 °C, the cutoff wavelength is close to that of the reported Ge material meaning that the Sn is completely segregated, agreeing well with the XRD, Raman and absorption results. In order to assess the photocurrent contribution from GeSn alloys and suppress photocurrent contributions from absorption by the Ge barrier layers and Ge virtual substrate, an undoped Ge wafer was used as a filter in front of each sample in the FTIR beam path. The rest of the experimental setup was kept the same as the response measurement setup. From Fig. 11 (c), it is clear that the response of the samples annealed from 200 °C to 400 °C is much improved compared to the as-grown sample, especially for the samples annealed at 400 °C. However, when we tried to observe the optical response of samples annealed above 500 °C, it was too weak for our experimental setup to detect due to the massive loss of Sn element in the GeSn layer. This phenomenon implies that Sn segregation seriously impacts the optical response for GeSn material. Fig. 11 (d) shows Photocurrent–Bias voltage characteristics of the MSM PDs based on the as-grown sample, and the samples annealed from 200 °C to 500 °C under incident light power P_{in} = 5 mW at λ = 1.55 μm. The photo-response of the samples annealed from 200 °C to 400 °C (the sample at 400 °C in particular) at 1.55 μm is much higher than that of the as-grown sample. The photo-response of the samples annealed above 500 °C is severely degraded, implying that Sn segregation and the disruption of the MQWs structure have a severe impact on the photo-response performance of the GeSn material, rather than just a narrowing of the response range.

To quantitatively compare the performance of the fabricated devices,

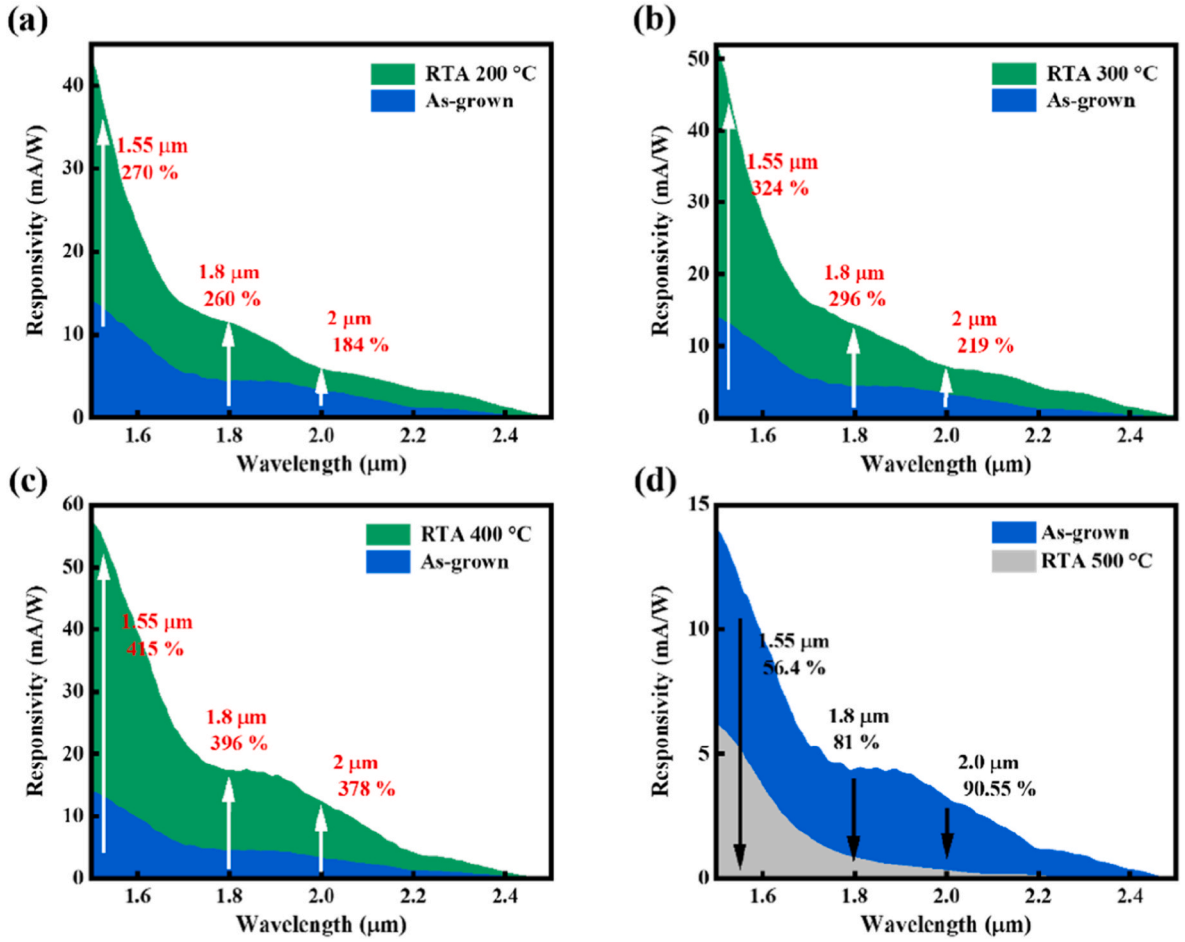

Fig. 12. (a)–(d) Comparison of responsivity between the as-grown sample and samples that are annealed at 200, 300, 400, and 500 °C, with the wavelength ranging from 1.5 μm to 2.5 μm and at a bias voltage of 1 V.

Fig. 12 (a)-(d) show the responsivity comparison between the as-grown and the annealed samples from 200 °C to 500 °C with 1.55 μm laser calibration. It is clear to see that the sample annealed at 400 °C has the highest responsivity among all the samples, indicating a higher absorption capability due to the crystal quality improvement in the wavelength range of 1.5 μm and 2.5 μm compared to other samples. It is thus evident that proper heat treatment can be applied to improve light absorption and optical response. Compared to the sample without RTA, the responsivity of the samples annealed at 400 °C shows a 415% improvement at 1.55 μm, a 396% improvement at 1.8 μm and a 378% improvement at 2.0 μm, respectively. This drastic responsivity improvement contributed to the improvement of material quality, consistent with the Raman FWHM and FTIR absorption results. However, for the samples annealed at 500 °C, the responsivity of the samples annealed at 500 °C shows a 56.4% degradation at 1.55 μm, an 81% degradation at 1.8 μm, and a 90.55% degradation at 2.0 μm, respectively. This phenomenon is attributed to Sn segregation and the disruption of the MQWs structure. In order to further enhance the responsivity of the GeSn/Ge MQWs MSM PDs while maintaining the structural integrity of GeSn/Ge MQWs, an appropriate annealing condition is required.

4. Conclusion

In Summary, high quality $Ge_{0.883}Sn_{0.117}$/Ge MQWs structure was grown on a Ge virtual substrate via low-temperature MBE techniques followed by RTA. We have performed a systematic study about the effect of RTA on the structural, optical and optoelectronic properties of the GeSn/Ge MQWs. XRD, TEM, AFM, SIMS and Raman characterizations manifest that the GeSn/Ge MQWs maintain coherently strained under RTA at 400 °C and lower. At higher annealing temperature, Sn segregation and interdiffusion of Ge and Sn atoms result in destruction of the MQWs structure. It was observed that GeSn well layers exhibit a maximum absorption window at 2.0–2.4 μm after RTA at 400 °C, and the absorption edge gradually moves to shorter wavelengths as the RTA temperature increases from 600 °C to 800 °C due to the severe Sn segregation. It is found that crystalline quality is improved after RTA at 400 °C, exhibiting the lowest dark current. Furthermore, the responsivity of the GeSn/Ge MQWs MSM PDs after RTA at 400 °C, with a cutoff wavelength 2.5 μm, can be effectively improved by 4.15 and 3.78 folds at 1.55 and 2 μm, capturing a wide range of the SWIR band. These findings reveal that the RTA process can be an effective approach for improving GeSn crystal quality and further enhancing the performance of SWIR photonic devices. This research paves the path for the high-performance monolithic and CMOS-compatible SWIR photonic devices.

CRediT authorship contribution statement

Haochen Zhao: Writing – review & editing, Writing – original draft, Investigation, Formal analysis, Data curation, Conceptualization. **Guangyang Lin:** Writing – review & editing, Methodology. **Chaoya Han:** Methodology, Formal analysis. **Ryan Hickey:** Methodology. **Tuofu Zhama:** Methodology. **Peng Cui:** Methodology. **Tienna Deroy:** Methodology. **Xu Feng:** Methodology. **Chaoying Ni:** Methodology, Formal analysis. **Yuping Zeng:** Writing – review & editing, Supervision.

Declaration of competing interest

The authors declare that they have no known competing financial interests or personal relationships that could have appeared to influence the work reported in this paper.

Data availability

Data will be made available on request.

Acknowledgments

This material is based upon work supported in part by Department of Energy, Office of Basic Energy of Sciences (EFRC) under Award No. DE-SC0023412, in part by the NASA with the Grant No. 80NSSC20M0142, 80NSSC22M0039, 80NSSC22M0171 and in part by Air Force Office of Scientific research with Award No. FA9550-22-1-0126. We thank Prof. James Kolodzey and Ryan Hickey for helpful discussions and suggestions on molecular beam epitaxy instrument repair and Zhaoquan Zeng for the insightful SIMS discussions.

Appendix A. Supplementary data

Supplementary data to this article can be found online at https://doi.org/10.1016/j.vacuum.2023.111868.

References

[1] M. Amani, C. Tan, G. Zhang, C. Zhao, J. Bullock, X. Song, H. Kim, V.R. Shrestha, Y. Gao, K.B. Crozier, M. Scott, A. Javey, Solution-synthesized high-mobility tellurium nanoflakes for short-wave infrared photodetectors, ACS Nano 12 (2018) 7253–7263, https://doi.org/10.1021/acsnano.8b03424.

[2] A.M. Hoang, A. Dehzangi, S. Adhikary, M. Razeghi, High performance bias-selectable three-color Short-wave/Mid-wave/Long-wave Infrared Photodetectors based on Type-II InAs/GaSb/AlSb superlattices, Sci. Rep. 6 (2016), 24144, https://doi.org/10.1038/srep24144.

[3] H. Cong, F. Yang, C. Xue, K. Yu, L. Zhou, N. Wang, B. Cheng, Q. Wang, Sandwich-like MoS_2@SnO_2@C with high capacity and stability for sodium/potassium ion batteries, Small 14 (2018), https://doi.org/10.1002/smll.201703818, 1704414-1703818.

[4] P. Martyniuk, J. Antoszewski, M. Martyniuk, L. Faraone, A. Rogalski, New concepts in infrared photodetector designs, Appl. Phys. Rev. 1 (2014), 041102, https://doi.org/10.1063/1.4896193.

[5] R.U. Martinelli, T.J. Zamerowski, P.A. Longeway, 2.6 μm InGaAs photodiodes, Appl. Phys. Lett. 53 (1998) 989–991, https://doi.org/10.1063/1.100050.

[6] K. Nishida, K. Taguchi, Y. Matsumoto, InGaAsP heterostructure avalanche photodiodes with high avalanche gain, Appl. Phys. Lett. 35 (1979) 251–253, https://doi.org/10.1063/1.91089.

[7] J. Rothman, L. Mollard, S. Bosson, G. Vojetta, K. Foubert, S. Gatti, G. Bonnouvrier, F. Salveti, A. Kerlain, O. Pacaud, Short-wave infrared HgCdTe avalanche photodiodes, J. Electron. Mater. 41 (2012) 2928–2936, https://doi.org/10.1007/s11664-012-1970-4.

[8] H. Cong, C. Xue, J. Zheng, F. Yang, K. Yu, Z. Liu, X. Zhang, B. Cheng, Q. Wang, Silicon based GeSn p-i-n photodetector for SWIR detection, IEEE Photonics J. 5 (2016) 1–6, https://doi.org/10.1109/JPHOT.2016.2607687.

[9] I.I. Izhnin, A.V. Voitsekhovsky, A.G. Korotaev, O.I. Fitsych, A.Y. Bonchyk, H. V. Savytskyy, K.D. Mynbaev, V.S. Varavin, S.A. Dvoretsky, N.N. Mikhailov, M. V. Yakushev, R. Jakiela, Optical and electrical studies of arsenic–implanted HgCdTe films grown with molecular beam epitaxy on GaAs and Si substrates, Infrared Phys. Technol. 81 (2017) 52–58, https://doi.org/10.1016/j.infrared.2016.12.006.

[10] Y. Dong, W. Wang, S. Lee, D. Lei, X. Gong, W. Loke, S. Yoon, G. Liang, Y. Yeo, Germanium-tin multiple quantum well on silicon avalanche photodiode for photodetection at two micron wavelength, Semicond. Sci. Technol. 31 (2016), 095001, https://doi.org/10.1088/0268-1242/31/9/095001.

[11] Y. Dong, W. Wang, X. Xu, X. Gong, D. Lei, Q. Zhou, Z. Xu, W. Loke, S. Yoon, G. Liang, Y. Yeo, Germanium-tin on Si avalanche photodiode: device design and technology demonstration, IEEE Trans. Electron. Dev. 62 (2015) 128–135, https://doi.org/10.1109/TED.2014.2366205.

[12] M. Coppinger, J. Hart, N. Bhargava, S. Kim, J. Kolodzey, Photoconductivity of germanium tin alloys grown by molecular beam epitaxy, Appl. Phys. Lett. 102 (2013), 141101, https://doi.org/10.1063/1.4800448.

[13] G. He, H.A. Atwater, Interband transitions in Sn_xGe_{1-x} alloys, Phys. Rev. Lett. 79 (1997) 1937–1940, https://doi.org/10.1103/PhysRevLett.79.1937.

[14] YuG. Sadofyev, V.P. Martovitsky, A.V. Klekovkin, V.V. Saraikin, I.S. Vasil'Evskii, Thermal stability of Ge/GeSn nanostructures grown by MBE on (001) Si/Ge virtual wafers, Phys. Procedia 72 (2015) 411–418, https://doi.org/10.1016/j.phpro.2015.09.078.

[15] D. Imbrenda, R.A. Carrasco, R. Hickey, N.S. Fernando, S. Zollner, J. Kolodzey, Band structure critical point energy in germanium–tin alloys with high tin contents, Appl. Phys. Lett. 119 (2021), 162102, https://doi.org/10.1063/5.0064358.

[16] G. Lin, P. Cui, T. Wang, R. Hickey, J. Zhang, H. Zhao, J. Kolodzey, Y. Zeng, Fabrication of germanium tin microstructures through inductively coupled plasma dry etching, IEEE Trans. Nanotechnol. 20 (2021) 846–851, https://doi.org/10.1109/TNANO.2021.3115509.

[17] B. Dutt, H. Lin, D.S. Sukhdeo, B.M. Vulovic, S. Gupta, D. Nam, K.C. Saraswat, J. S. Harris Jr., Theoretical analysis of GeSn alloys as a gain medium for a Si-compatible laser, IEEE J. Sel. Top. Quant. Electron. 19 (2013), https://doi.org/10.1109/JSTQE.2013.2241397, 1502706-1502706.

[18] G. Grzybowski, R.T. Beeler, L. Jiang, D.J. Smith, J. Kouvetakis, J. Menéndez, Next generation of $Ge_{1-y}Sn_y$ (y = 0.01-0.09) alloys grown on Si(100) via Ge_3H_8 and SnD_4: reaction kinetics and tunable emission, Appl. Phys. Lett. 101 (2012), 072105, https://doi.org/10.1063/1.4745770.

[19] H. Zhou, S. Xu, S. Wu, Y. Huang, P. Zhao, J. Tong, B. Son, X. Guo, D. Zhang, X. Gong, C.S. Tan, Photo detection and modulation from 1,550 to 2,000 nm realized by a GeSn/Ge multiple-quantum-well photodiode on a 300-mm Si substrate, Opt Express 28 (2020) 34772–34786, https://doi.org/10.1364/OE.409944.

[20] Y. Huang, G. Chang, H. Li, H.H. Cheng, Sn-based waveguide p-i-n photodetector with strained GeSn/Ge multiple-quantum-well active layer, Opt. Lett. 42 (2017) 1652–1655, https://doi.org/10.1364/OL.42.001652.

[21] N. Bhargava, M. Coppinger, J.P. Gupta, L. Wielunski, J. Kolodzey, Lattice constant and substitutional composition of GeSn alloys grown by molecular beam epitaxy, Appl. Phys. Lett. 103 (2013), 041908, https://doi.org/10.1063/1.4816660.

[22] C. Chi, L. Yue, Y. Zhang, Z. Zhang, X. Ou, S. Wang, Molecular beam epitaxy growth of $GaSb_{1-x}Bi_x$ without rotation, Vacuum 168 (2019), 108819, https://doi.org/10.1016/j.vacuum.2019.108819.

[23] D. Majchrzak, S. Gorantla, E. Zdanowicz, A. Pieniązek, J. Serafinczuk, K. Moszak, D. Pucicki, M. Grodzicki, B.J. Kowalski, R. Kudrawiec, D. Hommel, Detailed surface studies on the reduction of Al incorporation into AlGaN grown by molecular beam epitaxy in the Ga-droplet regime, Vacuum 202 (2022), 111168, https://doi.org/10.1016/j.vacuum.2022.111168.

[24] D. Imbrenda, R. Hickey, R.A. Carrasco, N.S. Fernando, J. VanDerslice, S. Zollner, J. Kolodzey, Infrared dielectric response, index of refraction, and absorption of germanium-tin alloys with tin contents up to 27% deposited by molecular beam epitaxy, Appl. Phys. Lett. 113 (2018), 122104, https://doi.org/10.1063/1.5040853.

[25] N.V.D. Driesch, S. Wirths, R. Troitsch, G. Mussler, U. Breuer, O. Moutanabbir, D. Grützmacher, D. Buca, Thermally activated diffusion and lattice relaxation in (Si)GeSn materials, Phys. Rev. Mater. 4 (2020), 033604, https://doi.org/10.1103/PhysRevMaterials.4.033604.

[26] P. Zaumseil, Y. Hou, M.A. Schubert, N.V.D. Driesch, D. Stange, D. Rainko, M. Virgilio, D. Buca, G. Capellini, The thermal stability of epitaxial GeSn layers, Apl. Mater. 6 (2018), 076108, https://doi.org/10.1063/1.5036728.

[27] H. Jia, P. Jurczak, J. Yang, M. Tang, K. Li, H. Deng, M. Dang, S. Chen, H. Liu, Impact of ex-situ annealing on strain and composition of MBE grown GeSn, J. Phys. D Appl. Phys. 53 (2020), 485104, https://doi.org/10.1088/1361-6463/abae94.

[28] D. Zhang, Y. Liao, J. Li, T. Wen, L. Jin, X. Wang, J. Kolodzey, Effect of in-situ annealing on the structural and optical properties of GeSn films grown by MBE, J. Alloys Compd. 684 (2016) 643–648, https://doi.org/10.1016/j.jallcom.2016.05.238.

[29] T.G.G. Maffeis, M.W. Penny, A. Castaing, O.J. Guy, S.P. Wilks, XPS investigation of vacuum annealed vertically aligned ultralong ZnO nanowires, Surf. Sci. 606 (2012) 99–103, https://doi.org/10.1016/j.susc.2011.09.007.

[30] X. Zhang, Z. Liu, C. He, B. Cheng, C. Xue, C. Li, Q. Wang, Characterization and thermal stability of GeSn/Ge multi-quantum wells on Ge (100) substrates, J. Mater. Sci. Mater. Electron. 27 (2016) 9341–9345, https://doi.org/10.1007/s10854-016-4974-7.

[31] G. Lin, K. Qian, H. Cai, H. Zhao, J. Xu, S. Chen, C. Li, R. Hickey, J. Kolodzey, Y. Zeng, Enhanced photoluminescence of GeSn by strain relaxation and spontaneous carrier confinement through rapid thermal annealing, J. Alloys Compd. 915 (2022), 165453, https://doi.org/10.1016/j.jallcom.2022.165453.

[32] L. Wang, Y. Zhang, Y. Wu, T. Liu, Y. Miao, L. Meng, Z. Jiang, H. Hu, Effects of annealing on the behavior of Sn in GeSn alloy and GeSn-based photodetectors, IEEE Trans. Electron. Dev. 67 (2020) 3229–3234, https://doi.org/10.1109/TED.2020.3004123.

[33] W. Wang, Y. Dong, Q. Zhou, E.S. Tok, Y. Yeo, Germanium–tin interdiffusion in strained Ge/GeSn multiple-quantum-well structure, J. Phys. D Appl. Phys. 49 (2016), 225102, https://doi.org/10.1088/0022-3727/49/22/225102/meta.

[34] C. Xue, X. Zhang, H. Cong, B. Cheng, Q. Wang, Si-based Ge and GeSn material epitaxy and thermal stability characterization, ECS Trans. 75 (2016) 257–262, https://doi.org/10.1149/07508.0257ecst/meta.

[35] H. Angermann, J. Rappich, L. Korte, I. Sieber, E. Conrad, M. Schmidt, K. Hubener, J. Polte, J. Hauschild, Wet-chemical passivation of atomically flat and structured silicon substrates for solar cell application, Appl. Surf. Sci. 254 (2008) 3615–3625, https://doi.org/10.1016/j.apsusc.2007.10.099.

[36] A. Gassenq, L. Milord, J. Aubin, N. Pauc, K. Guilloy, J. Rothman, D. Rouchon, A. Chelnokov, J.M. Hartmann, V. Reboud, V. Calvo, Raman spectral shift versus strain and composition in GeSn layers with 6%–15% Sn content, Appl. Phys. Lett. 110 (2017), 112101, https://doi.org/10.1063/1.4978512.

[37] Z.P. Zhang, Y.X. Song, Y.Y. Li, X.Y. Wu, Z.Y.S. Zhu, Y. Han, L.Y. Zhang, H. Huang, S.M. Wang, Effect of thermal annealing on structural properties of GeSn thin films

grown by molecular beam epitaxy, AIP Adv. 7 (2017), 105020, https://doi.org/10.1063/1.5005970.

[38] G. Greczynski, L. Hultman, A step-by-step guide to perform x-ray photoelectron spectroscopy, J. Appl. Phys. 132 (2022), 011101, https://doi.org/10.1063/5.0086359.

[39] G. Greczynski, L. Hultman, X-ray photoelectron spectroscopy: towards reliable binding energy referencing, Prog. Mater. Sci. 107 (2020), 100591, https://doi.org/10.1016/j.pmatsci.2019.100591.

[40] F. Yang, K. Yu, H. Cong, C. Xue, B. Cheng, N. Wang, L. Zhou, Z. Liu, Q. Wang, Highly enhanced SWIR image sensors based on $Ge_{1-x}Sn_x$-Graphene heterostructure photodetector, ACS Photonics 6 (2019) 1199–1206, https://doi.org/10.1021/acsphotonics.8b01731.

[41] G. Greczynski, L. Hultman, The same chemical state of carbon gives rise to two peaks in X-ray photoelectron spectroscopy, Sci. Rep. 11 (2021), 11195, https://doi.org/10.1038/s41598-021-90780-9.

[42] G. Greczynski, L. Hultman, Reliable determination of chemical state in x-ray photoelectron spectroscopy based on sample-work-function referencing to adventitious carbon: resolving the myth of apparent constant binding energy of the C 1s peak, Appl. Surf. Sci. 451 (2018) 99–103, https://doi.org/10.1016/j.apsusc.2018.04.226.

[43] D. Berlin, Fabricating Silicon Germanium Waveguides by Low Pressure Chemical Vapor Deposition, Massachusetts Institute of Technology, 2012.